

Research Article

Improving Electrochemical Activity in a Semi-V-I Redox Flow Battery by Using a C-TiO₂-Pd Composite Electrode

Tsung-Sheng Chen,¹ Shu-Ling Huang^{ID,1}, Mei-Ling Chen,² Tz-Jiun Tsai,¹ and Yung-Sheng Lin^{ID,1}

¹Department of Chemical Engineering, National United University, Miaoli 360, Taiwan

²Department of Electrical Engineering, National United University, Miaoli 360, Taiwan

Correspondence should be addressed to Shu-Ling Huang; simone@nuu.edu.tw and Yung-Sheng Lin; linys@nuu.edu.tw

Received 2 July 2018; Revised 29 October 2018; Accepted 8 November 2018; Published 20 January 2019

Guest Editor: Zhengping Zhou

Copyright © 2019 Tsung-Sheng Chen et al. This is an open access article distributed under the Creative Commons Attribution License, which permits unrestricted use, distribution, and reproduction in any medium, provided the original work is properly cited.

This study developed composite electrodes used in a semi-vanadium/iodine redox flow battery (semi-V-I RFB) system and designed semi-V-I RFB stacks to provide performance comparable to that of an all-vanadium redox flow battery (all-VRFB) system. These electrodes were modified using the electroless plating method and sol-gel process. The basic characteristics of the composited electrodes, such as the surface structural morphology, metal crystal phases, and electrochemical properties, were verified through cyclic voltammetry, field emission-scanning electron microscopy, energy-dispersive X-ray spectrometry, and X-ray diffraction. The results show that the sintering C-TiO₂-Pd electrode improved the electrocatalytic activity of the semi-V-I RFB system, thereby effectively increasing the energy storage ability of the system. The C-TiO₂-Pd electrode was used as a negative electrode in a single semi-V-I RFB and exhibited excellent cyclic performance in a charge-discharge test of 50 cycles. The average values for coulomb efficiency, voltage efficiency, and energy efficiency were approximately 96.56%, 84.12%, and 81.23%, respectively. Moreover, the semi-V-I RFB stacks were designed using series or parallel combination methods that can effectively provide the desired operating voltage and linearly increase the power capacity. The amount of vanadium salt required to fabricate the semi-V-I RFB system can be reduced by combining large stack modules of the system. Therefore, this system not only reduced costs but also exhibited potential for applications in energy storage systems.

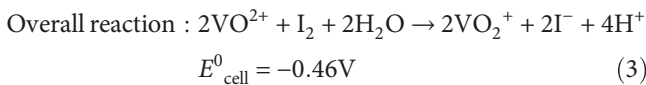
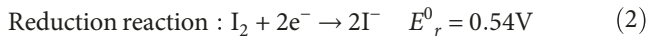
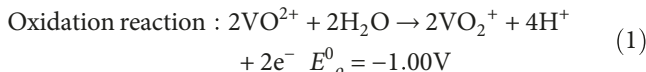
1. Introduction

The energy of a redox flow battery (RFB) is stored in separated positive and negative electrolytes, which provide the driving force that initiates the oxidation-reduction reaction [1]. The use of energy stored in the form of chemical energy, a mode of storage that does not entail any geographical restrictions, is expected to facilitate large-scale energy storage and has significant environmental and socioeconomic advantages. RFBs have been utilized as large-scale energy storage systems in the last decade [2–5]. The all vanadium RFB (all-VRFB) is one of the most promising technologies for mid-to-large-scale (kilowatt-megawatt) energy storage and was first proposed by Skyras-Kazacos in 1985 [6, 7]. The power output of a vanadium RFB increases with the size of the cell stack and the active electrode surface area, whereas

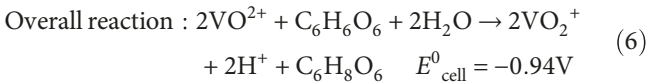
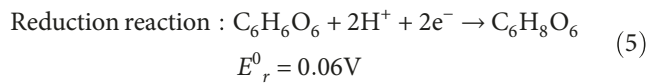
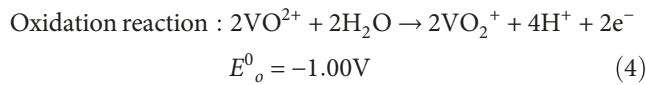
its energy storage capacity increases with the volume of the storage tanks and the electrolyte concentrations [8–10]. The all-VRFB can be modified for use in specific large-scale utility applications; however, these batteries are more expensive than secondary batteries. Consequently, the technologies of the all-VRFB system should be further advanced to realize low-cost fabrication and to improve performance and durability, thus enabling their widespread application. The key materials of the all-VRFB system include an ion exchange membrane, electrodes, electrolyte, and a flow channel. The battery's energy density is determined not only by the characteristics of these key materials but also by their intimate interrelationships. An ideal electrode is one that exhibits low resistance, high conductivity, and acid-resisting property. Many studies have focused on modifying electrode materials, such as increasing their electrocatalytic activity or developing

a new, low-cost electrode with more robust mechanical strength in concentrated acid solutions [11–15]. In our previous research, we developed a novel semi-vanadium-iodine RFB (semi-V-I RFB) [16]. This battery has a high coulomb efficiency and significantly reduces the fabrication cost; however, its voltage efficiency is low (68%). The overall reactions of vanadium-iodine, iodine-vitamin C ($C_6H_8O_6$), and vanadium-vitamin C oxide ($C_6H_6O_6$) can be expressed as shown in equations (1)–(6) on the charging mode.

1.1. Vanadium-Iodine.



1.2. Vanadium-Vitamin C.



A study demonstrated that the reversibility of the oxidation-reduction reaction can be effectively increased if vitamin C is added to the iodine solution [17]. Therefore, the standard electromotive forces of the semi-V-I RFB system are between 0.46 to 0.94 V on the discharging mode.

This study focused on developing composite electrodes that can be used as the negative electrode of the semi-V-I RFB system to effectively improve the voltage efficiency of the system. Furthermore, we designed semi-V-I RFB stacks and compared the charge-discharge performance of the stacks with that of the all-VRFB system.

2. Experimental

2.1. Fabrication of Composite Electrodes. Graphite carbon paper electrodes (C-electrodes; Shenhe Carbon Fiber Materials Co. Ltd., Liaoning, China) were modified by depositing palladium (Pd) through electroless plating. The effective exposed surface area of the electrodes was $5 \times 5 \text{ cm}^2$. SnCl_2 and PdCl_2 were used as sensitized and active reagents in the deposition of the C-Pd electrode. The composition of the plating solution was 19 g/L $\text{Na}_2\text{C}_4\text{H}_4\text{O}_4 \cdot 6\text{H}_2\text{O}$, 10 g/L PdCl_2 , 8.5 g/L HCl, and 25.6 g/L $\text{C}_2\text{H}_4(\text{NH}_2)_2$. The C-Pd, C-Pd-TiO₂, and C-TiO₂-Pd electrodes were prepared through electroless metal deposition by using the composition of the

plating solution [18–21]. Among them, the C-TiO₂ electrode was fabricated using the following steps: tetrabutyrin acid was mixed with EtOH/HCl (pH = 1) aqueous solution at a tetrabutyrin acid : EtOH : HCl molar ratio of 1 : 8 : 4 in a flask and mechanically stirred to carry out the hydrolysis reaction at room temperature. Then, carbon paper was added to the pre-mixed tetrabutyrin acid solution under vigorous stirring for 1 h. Finally, it was completely dried in an oven at 60°C, and a C-TiO₂ composite electrode was obtained. The C-Pd-TiO₂ and C-TiO₂-Pd electrodes were fabricated using a two-step deposition method. In the first step, the sol-gel route was employed to prepare the C-TiO₂-electrode, following which the Pd was redeposited on the C-TiO₂ electrode through the electroless technique to form the C-TiO₂-Pd modified electrode. The C-Pd-TiO₂ electrode was fabricated under the same conditions, but with the process reversed. The plating solution had a pH in the range of 4.8–5.1 at 80°C. Finally, the modified electrodes were heat treated at 400°C in an oven for 1 h. All chemicals used were of analytical reagent grade.

2.2. Morphology and Composition of Composite Electrodes. The surface morphologies and components of the composite electrodes were characterized through scanning electron microscopy coupled with energy dispersive X-ray analysis (JSM-6700F, JEOL, Tokyo, Japan). The composition of the electrode was identified through X-ray diffraction (XRD) with a filtered Cu-Ka radiation source (X'Pert PRO, PANalytical, Almelo, the Netherlands), and diffraction patterns were collected from 20° to 90°.

2.3. Measurement of the Electrochemical Properties. Cyclic voltammetry (CV) experiments were conducted in a three-electrode cell and by using an electrochemical analyzer (CHI 6273 C, CH Instruments Inc., US). The composition of the cell was as follows: an Ag-AgCl electrode was used as the quasireference electrode, the reference electrode and the platinum gauze were used as the counter electrode, and the C-Pd or C-TiO₂-Pd modified electrode with a surface area of $1 \times 1 \text{ cm}^2$ was used as the working electrode. The positive electrolyte was a solution of 0.01 M I₂ with a variable amount of vitamin C. The scan rate was varied from 1 to 10 mV·s⁻¹. Electrochemical properties, such as the potential interval (ΔE_p), ratio of the anodic-cathodic current (I_{pa}/I_{pc}), diffusion coefficient (D_o), and double-layer charged capacity (C_d), were obtained from the CV experimental data.

2.4. Charge-Discharge Test. We used the iodine-vitamin C solution as a cathode electrolyte and vanadium ion ($V^{4+}-V^{5+}$) solution as an anodic electrolyte to set up a single cell. The ($V^{4+}-V^{5+}$) vanadium solutions were prepared by dissolving 1 M VOSO₄ in 2 M H₂SO₄ aqueous solution. Multiple electrodes, that is, C and C-TiO₂-Pd electrode, were used. The electrodes were separated by a cationic exchange Nafion 117 membrane (DuPont, USA). In addition, the charge-discharge test was conducted on two cell stacks—series and parallel.

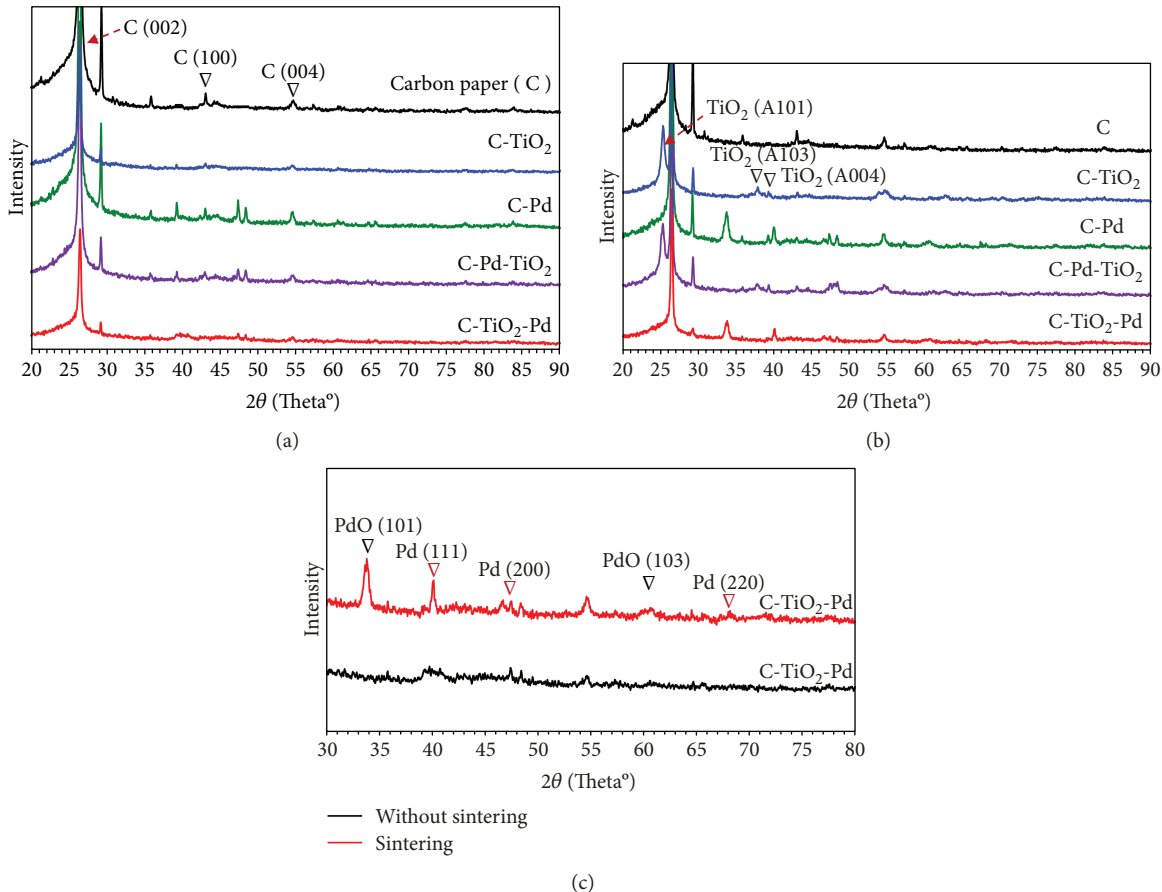


FIGURE 1: XRD patterns of various electrodes (a) without sintering for all electrodes, (b) sintering for all electrodes, and (c) without and with sintering for the C-TiO₂-Pd electrode.

3. Results and Discussion

3.1. Crystal Structure Identification of Composite Electrodes. The XRD diffraction patterns of all the composite electrodes, including C, C-TiO₂, C-Pd, C-Pd-TiO₂, and C-TiO₂-Pd with and without 400°C sintering, are shown in Figure 1. The diffraction pattern in Figure 1 reveals that (1) before sintering, C (002) possessed two sharp diffraction peaks at 27°–29° and two weak peaks, C (100)/C (004), at 43° and 54°, respectively. TiO₂ in the C-TiO₂ region was amorphous; thus, the diffraction patterns were similar to those of C. The (111), (200), and (220) facets of Pd with a face-centered cubic lattice structure were assigned to the diffraction peaks at 40°, 47°, and 68°, respectively. Three regions (i.e., C-Pd, C-Pd-TiO₂, and C-TiO₂-Pd) can verify a part of the Pd crystal structure (111, 200); nevertheless, the intensity of the peaks was weak in the C-TiO₂-Pd regions, as depicted in Figure 1(a). (2) After sintering, the C electrode's diffraction patterns remained unchanged. The C-TiO₂ electrode exhibited a strong diffraction peak at 25°, which was the anatase lattice structure of TiO₂ (A101), and a relatively weak diffraction peak at 38°–39° for TiO₂ (A103) and TiO₂ (A004). In the C-Pd-TiO₂ region, fingerprint peaks similar to those of TiO₂ were observed; however, these were not

observed in the C-TiO₂-Pd region. In particular, in the C-Pd and C-TiO₂-Pd regions, a strong new diffraction peak appeared at 34°, which is the diffraction characteristic peak of PdO (101), implying that Pd oxidized to form PdO, as presented in Figure 1(b). (3) A significant difference was observed between the diffraction peaks of C-TiO₂-Pd crystal structures with and without sintering. The intensity of the diffraction peaks of Pd (111) and Pd (200) for the sintering C-TiO₂-Pd electrode was stronger and more stable, and the diffraction pattern of Pd (220) was more apparent than without sintering. Moreover, a strong new PdO (101) diffraction peak was observed at 34° in the C-TiO₂-Pd regions but not in the C-Pd-TiO₂ region, as shown in Figure 1(c). Thus, the experimental results demonstrate that the stable Pd metals and PdO crystal structures for the C-TiO₂-Pd electrode could be formed through high-temperature sintering. These may affect electrocatalytic activity and generate different electrochemical properties [22–24].

3.2. Surface Morphology Analysis of Composite Electrodes. The scanning electron microscopy (SEM) images of the composite electrodes are presented in Figure 2. The Pd particles with white spots were deposited onto the carbon

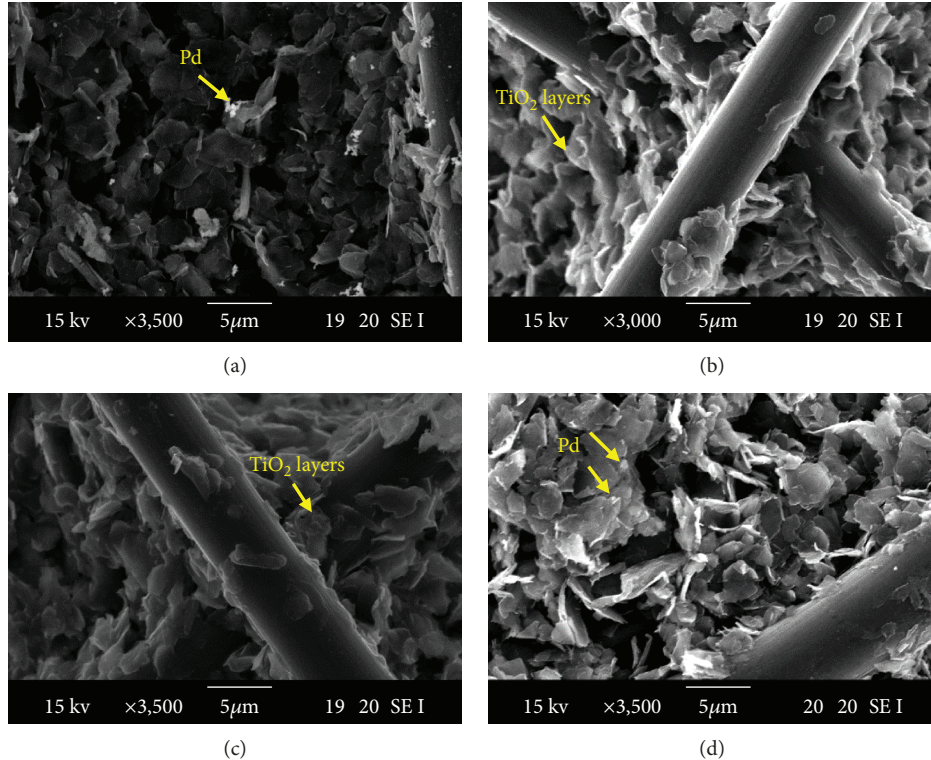


FIGURE 2: SEM images of composite electrodes. (a) C-Pd, (b) C-TiO₂, (c) C-Pd-TiO₂, and (d) C-TiO₂-Pd.

fiber layers of the C-Pd electrode and onto the TiO₂ layers of the C-TiO₂-Pd electrode, as shown in Figures 2(a) and 2(d). Nevertheless, we did not observe the Pd particles in the C-Pd-TiO₂ electrode in Figure 2(c), implying that the inner Pd particles are covered by the outer TiO₂ layers. Additionally, we observed that the growth in TiO₂ was derived from the inner layer and layer-by-layer stacking of TiO₂, and a significant number of TiO₂ grains were uniformly embedded into the carbon paper network matrix through the sol-gel method, as presented in Figure 2(b). Furthermore, to identify the component of the C-TiO₂-Pd electrode, we performed energy-dispersive spectrometry (EDS) analysis of the C-TiO₂-Pd electrode with sintering, as depicted in Figure 3. The spectrum and element analysis presented in Figure 3(a) reveals that the elements of the sintering C-TiO₂-Pd electrode included C (47.58 wt%), Ti (17.64 wt%), Pd (2.71 wt%), and O (32.07 wt%). O elements exhibited a high wt% under a low wt% Ti element, implying that Pd was oxidized to form PdO. These results were confirmed because the PdO (101) facet was assigned to the diffraction peak at 34°, as presented in Figure 1(c). In addition, the Pd particles were deposited uniformly on the TiO₂ layers, as illustrated in the mapping analysis of Figures 3(b)–3(f). The deposition of Pd and PdO particles on the TiO₂ layers reduced the aggregation of Pd particles and increased the active area of the C-TiO₂-Pd composite electrode.

3.3. Electrochemical Characteristics of Various Electrodes.

The CV curves of various electrodes in 10 mL of 0.01 M

iodine with 1 wt% vitamin C solution at a 10 mV/s scanning rate in the range of 0–1 V are shown in Figure 4, and the data are summarized in Table 1. The oxidation pattern of electrolyte solutions is referred to as an oxidized or anodic current peak (I_{pa}) on a tested electrode, corresponding to the anodic voltage (E_{pa}) when CV is scanned from a low to high potential. Conversely, if it is scanned from a high to low potential, then the electrolyte is reduced to obtain a reduced or cathodic current peak (I_{pc}) and a cathodic voltage (E_{pc}). The I_{pa}/I_{pc} ratio tended to unity, revealing that the quasireversible redox reactions occurred because of the effects of the iodine electrolyte solutions on the tested electrodes. The values of I_{pa} and I_{pc} were low, meaning that the redox efficiency of the composite electrodes in the iodine solutions was poor. The I_{pa} values were in the following order: C-TiO₂-Pd > C-Pd > C-Pd-TiO₂ > C > C-TiO₂. Moreover, the potential interval (ΔE_p) was in the following order: C-TiO₂ > C-Pd-TiO₂ > C-Pd > C > C-TiO₂-Pd, as listed in Table 1. The low ΔE_p value demonstrated that the energy barriers of redox reactions were lower because of the effects of the iodine electrolyte solutions on the tested electrodes. These results imply that the C-TiO₂-Pd electrode has higher redox currents and lower ΔE_p than other electrodes. Moreover, the C-TiO₂-Pd electrode had a symmetric I_{pa}/I_{pc} value, which was close to unity, meaning that this is a reversible redox reaction for the iodine solutions. In addition, the outer TiO₂ layer of the C-Pd-TiO₂ electrodes could not improve the redox kinetic reaction of the iodine solution; thus, the redox current of the C-Pd-TiO₂ electrode was lower

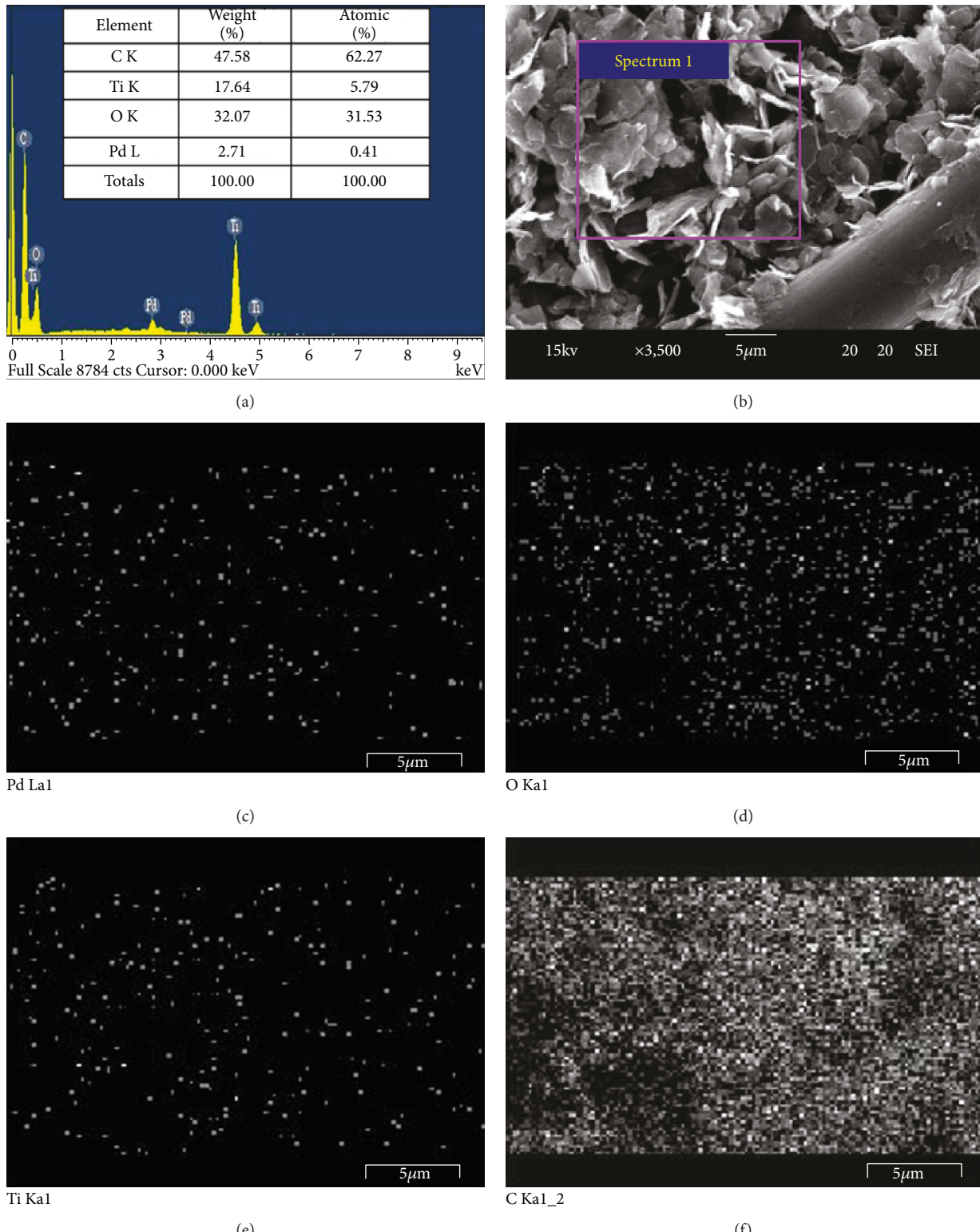


FIGURE 3: Analysis of energy-dispersive spectrometry (EDS) for the C-TiO₂-Pd electrode with sintering. (a) EDS spectrum and element analysis, (b) EDS mapping electron image, (c) Pd element, (d) O element, (e) Ti element, and (f) C element.

than that of the C-TiO₂-Pd electrode. Therefore, TiO₂ particles between a carbon matrix and Pd metal layers increase the active surface area of an electrode and can enhance

the electrocatalytic effect of the electrode [19, 22]. Consequently, the C-TiO₂-Pd electrode performed better in the redox kinetic reaction than the others.

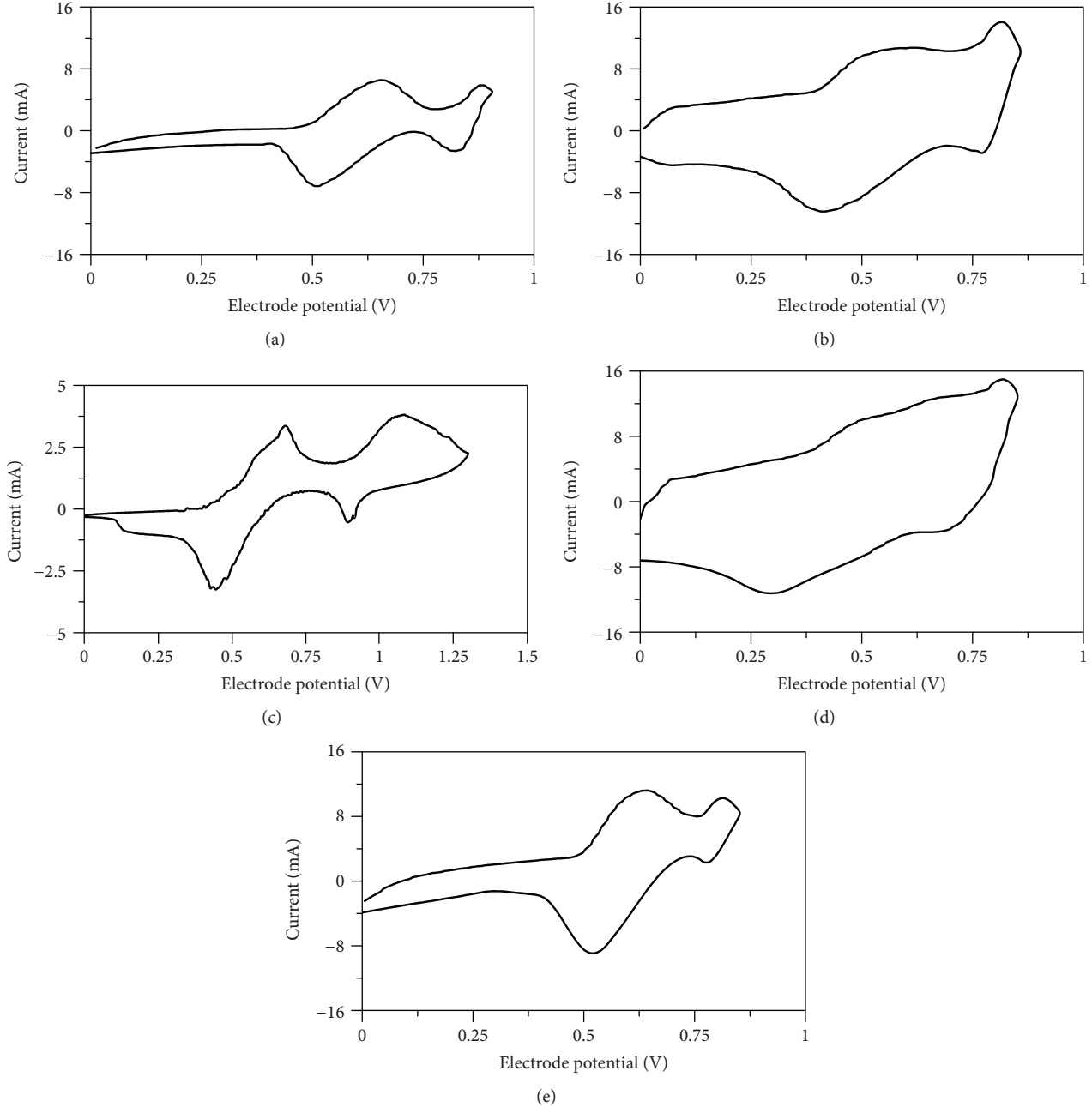


FIGURE 4: Cyclic voltammograms for 0.01 M iodine solution with 1 wt% of vitamin C on different electrodes: (a) C, (b) C-Pd, (c) C-TiO₂, (d) C-Pd-TiO₂, and (e) C-TiO₂-Pd.

3.4. Kinetic Reactions of Composite Electrodes. A reversible redox equation (7) can be obtained on the basis of the Randles–Sevcik equations [25, 26]:

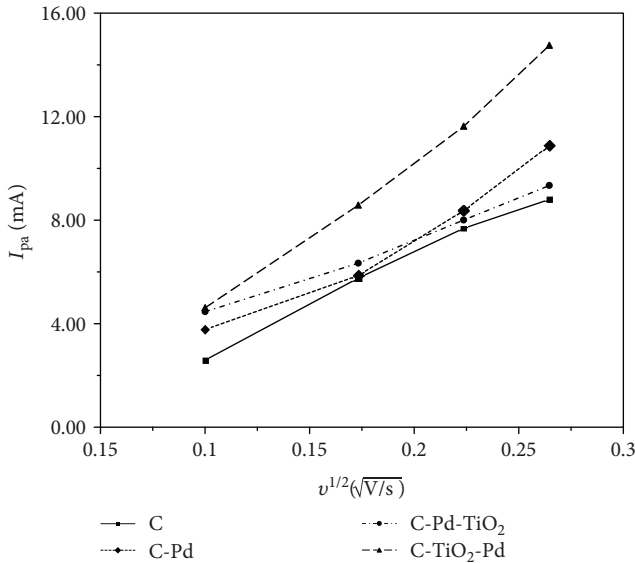
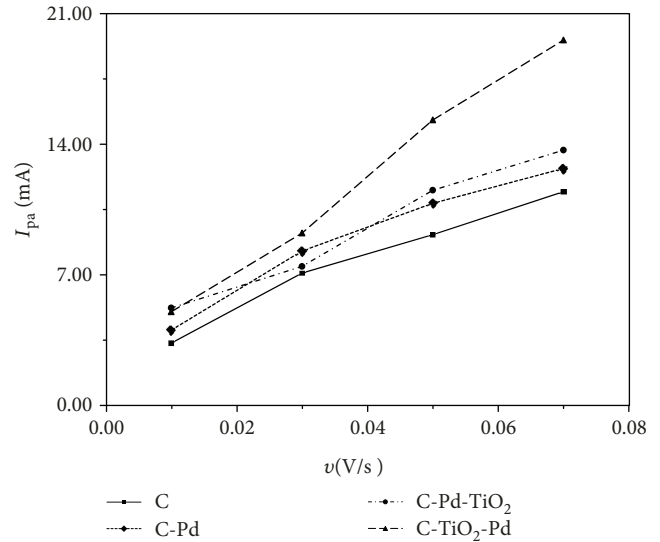
$$i_p = (2.69 \times 10^5) n^{3/2} ACD_o v^{1/2}, \quad (7)$$

where i_p , n , A , C , D_o , and v are the peak current, electron mobility number, reaction area (cm^2), concentration of reactants (mole/cm^3), diffusion coefficient (cm^2/s), and scan rate (V/s), respectively. The kinetic reactions of iodine with

vitamin C electrolyte solutions on various electrodes were studied through a series of CV experiments at different scan rates. The relationship between I_{pa} and $v^{1/2}$ was plotted in Figure 5, and the value of D_o was obtained using the slope of I_{pa} and $v^{1/2}$ and Randles–Sevcik equations [16]. As shown in Table 2, the modified C-TiO₂-Pd electrode increased the overall mass transfer and iodide ion electrochemical activity. The D_o value of iodine-vitamin C species was enhanced by approximately 60% compared with that of the C-electrode, from 12.8×10^{-6} to $20.4 \times 10^{-6} \text{ cm}^2/\text{s}$, on the C-TiO₂-Pd electrode.

TABLE 1: Cyclic voltammograms of 0.01 M iodine solutions with 1 wt% of vitamin C on different electrodes.

Electrodes	E_{pa} (V)	E_{pc} (V)	ΔE_p (V)	Anodic peak, I_{pa} (mA)	Cathodic peak, I_{pc} (mA)	I_{pa}/I_{pc}
C electrode	0.67	0.50	0.17	5.76	7.08	0.81
C-Pd electrode	0.61	0.42	0.19	5.86	8.27	0.71
C-TiO ₂ electrode	0.68	0.46	0.22	3.35	3.78	0.89
C-Pd-TiO ₂ electrode	0.50	0.29	0.21	6.34	7.44	0.85
C-TiO ₂ -Pd electrode	0.64	0.52	0.12	8.58	9.23	0.92

FIGURE 5: Plots of the anodic peak current (I_{pa}) versus the square root of scan rates ($v^{1/2}$) for the iodine-1 wt% vitamin C electrolyte for different electrodes.FIGURE 6: Plots of the anodic peak current (I_{pa}) versus the scan rate (v) for the iodine-vitamin C electrolyte for various electrodes.TABLE 2: D_0 and C_d of the iodine-vitamin C electrolyte solution on various electrodes.

Electrodes	$D_0 \times 10^6$ (cm^2/s)	C_d (F/cm^2)
Iodine/1 wt% vitamin C electrolytes	Iodine/1 wt% vitamin C electrolytes	
C electrode	12.8	0.132
C-Pd electrode	14.3	0.143
C-Pd-TiO ₂ electrode	9.9	0.148
C-TiO ₂ -Pd electrode	20.4	0.249

An electric double layer exists between the electrode and electrolyte. The electric double layer capacitor can be represented by equation (8).

$$i_{cd} = AC_d v, \quad (8)$$

where i_{cd} , A , C_d , and v are the electric double layer charging current, reaction area (cm^2), electric double layer capacitor

value (F/cm^2), and scan rate (V/s), respectively. On the basis of our previous research [16], the relationship between i_{cd} and v can be derived by forming a straight line with the slope proportional to C_d in Figure 6 for the iodine-vitamin C electrolyte for the different electrodes. Table 2 summarizes the C_d data for comparison. C_d was the highest for the C-TiO₂-Pd electrode in the iodine-vitamin C electrolyte. Moreover, C_d increased from 0.132 to 0.249 F/cm^2 , 89% higher than the C_d for the C-electrode.

3.5. Charge-Discharge Performance. Battery energy storage systems entail numerous design requirements, such as high voltage, current, power, and capacity. The capacity units of a large-scale energy storage battery system should meet the commercial operation requirements of the unit cells. Ordinarily, these batteries are fabricated in series or parallel to increase the storage capacity of the battery module and supply voltage group for achieving commercial requirements. In this section, we fabricated the C-TiO₂-Pd composite electrode as a negative electrode in the semi-V-I RFB system to design a single cell and series and parallel cell stacks and to evaluate the charge-discharge performance of the cell and stacks.

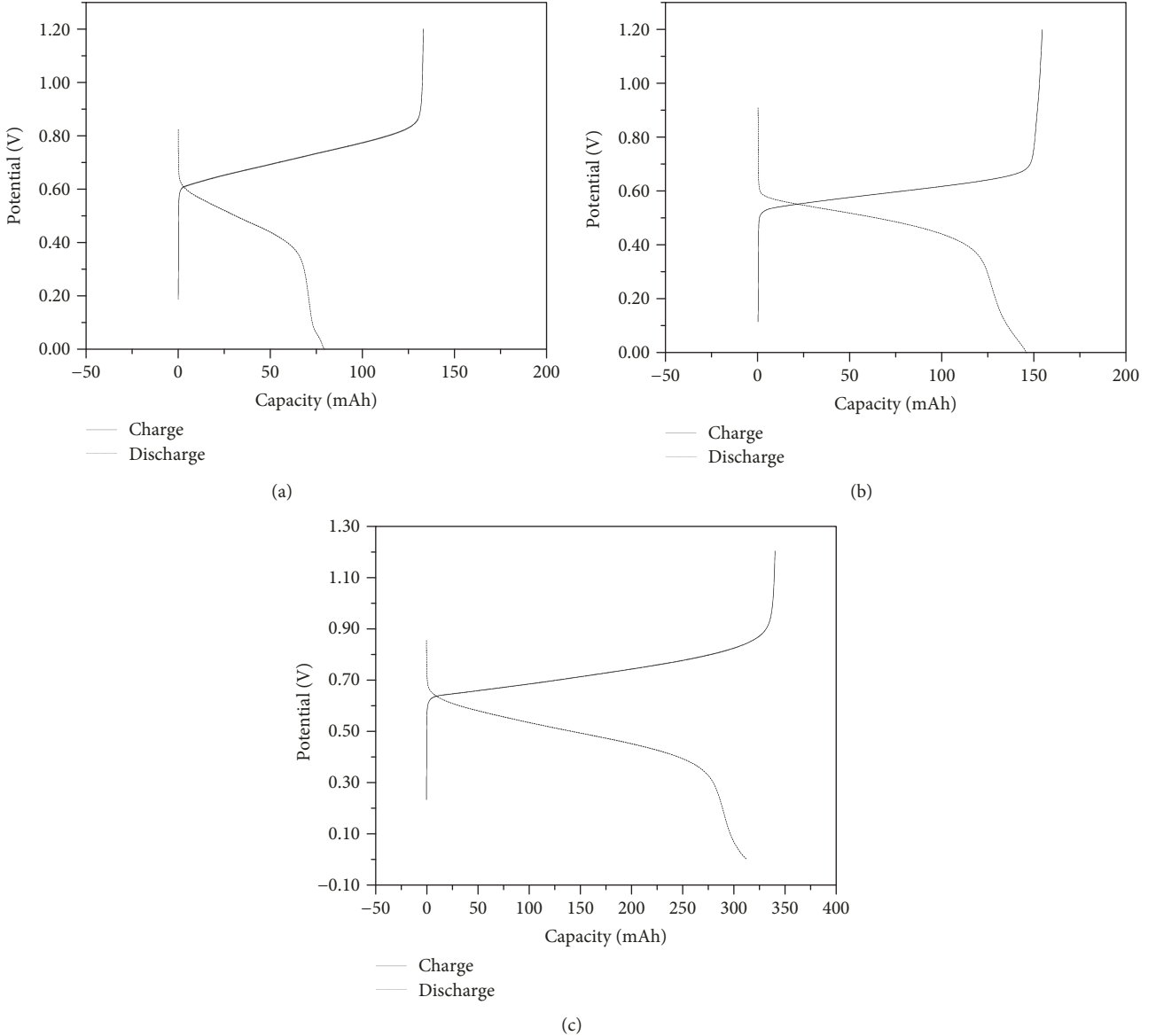


FIGURE 7: Charge-discharge diagrams of a semi-V-I RFB system with Nafion 117 as a separated membrane, C-TiO₂-Pd composite electrode as a negative electrode, and carbon paper as a positive electrode at different electrolyte concentrations. The volume of the electrolytic solution in each half cell was 10 mL. (a) 0.5 M I_2 ; (b) 1 M I_2 ; and (c) 2 M I_2 .

3.5.1. Single Cell. The RFB energy storage capacity is proportional to the volume and concentration of the electrolyte. The C-TiO₂-Pd composite electrode is employed as a negative electrode in the semi-V-I RFB system with various concentrations of the electrolyte to conduct the charge-discharge tests. The charge-discharge curves are displayed in Figure 7, and performance of a single semi-V-I RFB is detailed in Table 3. The data in Table 3 verify that the energy storage capacity of the semi-V-I RFB system increases with the concentration of iodine-vitamin C solutions. The system exhibited optimal performance in the 1 M iodine solution; the coulomb efficiency (CE), voltage efficiency (VE), and energy efficiency (EE) were 96%, 81%, and 77%, respectively.

TABLE 3: Charge-discharge performance of the semi-V-I RFB system at different electrolyte concentrations.

Iodine concentration (M)	Capacity (mAh)	CE (%)	VE (%)	EE (%)
0.5	70	60	66	39
1	130	96	81	77
2	280	92	67	62

As specified in the literature [19, 23, 24], crystal structures of metals or alloys have different effects on the catalytic electrode. In our study, we observed that C-TiO₂-Pd

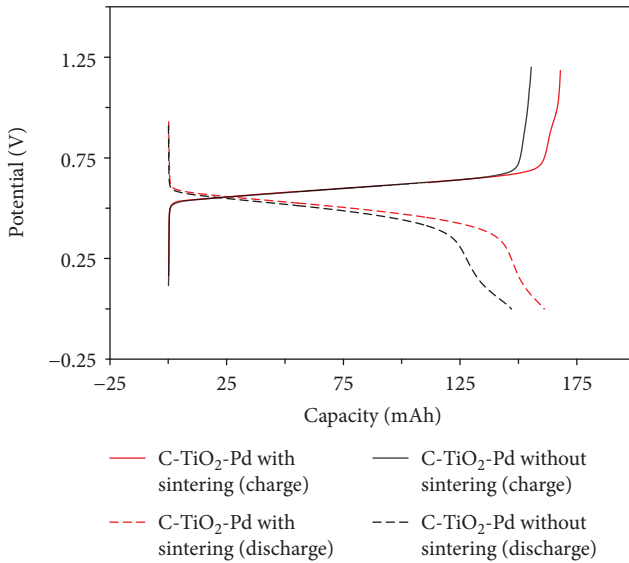


FIGURE 8: Charge-discharge diagram of the C-TiO₂-Pd electrodes by heat treatment for a semi-V-I RFB system.

TABLE 4: Charge-discharge performance of the C-TiO₂-Pd electrode by heat treatment for the semi-V-I RFB system.

Electrodes	Capacity (mAh)	CE (%)	VE (%)	EE (%)
C-TiO ₂ -Pd without sintering	130	96	81	77
C-TiO ₂ -Pd with sintering	150	96	87	83

electrodes with or without sintering at a high temperature affect the battery energy storage efficiency. Figure 8 displays the charge-discharge diagram of C-TiO₂-Pd electrodes with or without sintering in a semi-V-I RFB system, and the charge-discharge performance of the electrodes is detailed in Table 4; these data confirm that when the C-TiO₂-Pd electrode is sintered at high temperatures, the intensity of crystalline lattice conformations of Pd (111) and Pd (200) is stronger than that without sintering; additionally, a new PdO (101) crystal compound appeared, as shown in Figure 1(c). The formation of Pd (111), Pd (200), and PdO may contribute to the electrocatalytic activity in semi-V-I-RFB systems, in turn causing the VE to increase from 81% to 87% and EE from 77% to 83%. Furthermore, a series of continued charge-discharge tests of the semi-V-I RFB system was performed at a current density of 20 mA cm⁻² and is presented in Figure 9, which plots CE, VE, and EE as a function of cycle number. The average CE, VE, and EE values of the semi-V-I RFB system for 50 cycles illustrated in Figure 9 are approximately 96.52%, 84.12%, and 81.22%, respectively, revealing that the cyclic performance is excellent.

3.5.2. Battery Stacks. To facilitate large-scale commercial applications, the stacks of the RFB system are often fabricated in series and parallel cross combinations for increasing the storage capacity and operating voltage of the battery module.

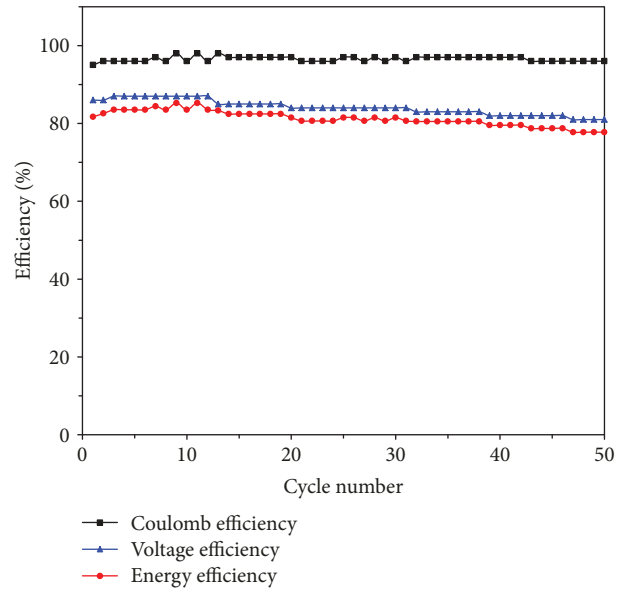


FIGURE 9: Cyclic efficiency diagram for a semi-V-I RFB system with Nafion 117 as a separated membrane, a C-TiO₂-Pd composite electrode as a negative electrode, and carbon paper as a positive electrode with a 1 M iodine/1 wt% vitamin C negative electrolyte and a 1 M VOSO₄/2 M H₂SO₄ positive electrolyte, and a current density of 20 mA cm⁻².

In the series configuration, the current supplied to the circuit is equal to the current across all elements in series ($I = I_1 = I_2 = \dots = I_N$), the total voltage is equal to the sum of each element voltage ($E = V_1 + V_2 + \dots + V_N$), and the total resistance is equal to the sum of each element resistance ($R_t = R_1 + R_2 + \dots + R_N$). In the parallel configuration, the total current is equal to the sum of each element current ($I_t = I_1 + I_2 + \dots + I_N$), the voltage supplied to the circuit is equal to the voltage across all elements in parallel ($V_t = V_1 = V_2 = \dots = V_N$), and the reciprocal of the total resistance is equal to the sum of the reciprocal of each element resistance ($1/R_t = 1/R_1 + 1/R_2 + \dots + 1/R_N$).

The charge and discharge curves of the all-VRFB stacks and the semi-V-I RFB stacks were composed of two cells in series and parallel, as shown in Figures 10(a) and 10(b), and the performances of the cells are summarized in Table 5. The results revealed that the charging voltage in the series stacks effectively increased from 1.8 to 3.6 V for the all-VRFB stacks, and the CE of the all-VRFB stacks significantly reduced to 73%. In the semi-V-I RFB system, a linear increase in the charging voltage from 1.2 to 2.4 V was observed. Moreover, the CE of the stacks remained at 92%, but the storage capacity of both systems was reduced. By comparison, in the series configuration, the overall efficiency value of the semi-VRFB system is higher than that of the all-VRFB system. In the parallel configuration, the capacity of the all-VRFB and semi-V-I RFB systems were altered from 139 to 137 mAh and from 147 to 162 mAh, respectively. The capacity of the semi-V-I RFB system improved slightly, but capacity of the all-VRFB system reduced. The charge-discharge performances of both systems attenuated significantly.

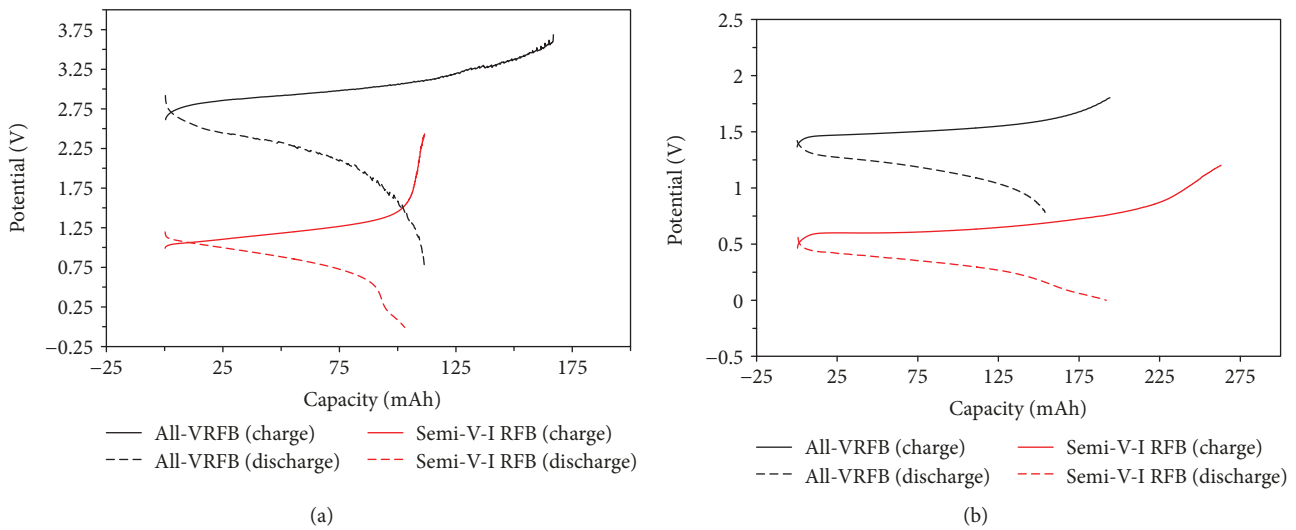


FIGURE 10: Charge-discharge diagram of all-VRFB and semi-V-I RFB stacks: (a) two cells in series and (b) two cells in parallel.

TABLE 5: Charge-discharge performance of all-VRFB and semi-V-I RFB stacks.

Types of battery		CE (%)	VE (%)	EE (%)	Capacity (mAh)	Charge voltage (V)
Single cell	All-VRFB	79	78	62	139	1.80
	Semi-V-I RFB	96	87	83	147	1.20
Series of two cells	All-VRFB	73	57	41	100	3.60
	Semi-V-I RFB	92	73	67	100	2.40
Parallel of two cells	All-VRFB	65	69	45	137	1.80
	Semi-V-I RFB	73	57	41	162	1.20

The capacity of the battery with the parallel combination cannot be increased; this may be due to the flow channel differences of the two batteries or due to an external line loss. If the voltage, inherent resistance, or current of the battery stacks are different, then a small voltage or battery resistance forms an electricity load and consumes part of the energy of another battery, thus decreasing the overall efficiency.

4. Conclusions

The C-TiO₂-Pd composite electrode was fabricated using carbon paper as a substrate that was coated with titanium dioxide and palladium metal in sequence. The C-TiO₂-Pd composite electrode exhibited superior electrochemical activity after high-temperature sintering. Moreover, the D_o value of the iodine-vitamin C electrolyte solutions increased by approximately 60% more than that of the C-electrode. The use of C-TiO₂-Pd as a negative electrode for the semi-V-I RFB system effectively enhanced the VE, thus improving the overall EE to 83%. In the series configuration, the charge voltage of the all-VRFB and semi-V-I RFB battery stacks linearly increased. However, performance of the all-VRFB battery stacks was significantly attenuated, and the EE decreased from 62% to 41%. By comparison, the semi-V-I RFB stacks can still be maintained at 67%. If we can use the design and assembly technology to enhance

and improve the flow channel of the battery, the overall efficiency can be effectively improved. For series and parallel combinations obtained by stacking large modules, the proposed semi-V-I RFB system has high application potential to meet commercial requirements.

Data Availability

Previously reported experiment system was used to support this study and is available at <https://www.hindawi.com/journals/jchem/2017/4590952/>. This prior study is cited within the text as reference [4].

Conflicts of Interest

The authors declare no conflicts of interest.

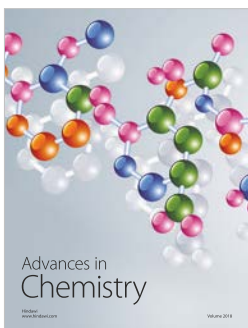
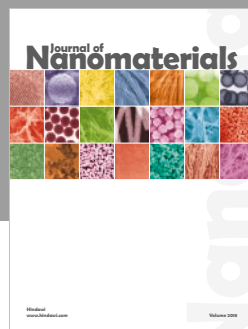
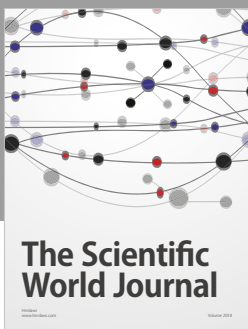
Acknowledgments

The authors are grateful for the financial support by the Ministry of Science and Technology, Taiwan.

References

- [1] P. Alotto, M. Guarneri, and F. Moro, "Redox flow batteries for the storage of renewable energy: a review," *Renewable and Sustainable Energy Reviews*, vol. 29, pp. 325–335, 2014.

- [2] A. Cunha, J. Martins, N. Rodrigues, and F. P. Brito, "Vanadium redox flow batteries: a technology review," *International Journal of Energy Research*, vol. 39, no. 7, pp. 889–918, 2015.
- [3] J. Xi, S. Xiao, L. Yu, L. Wu, L. Liu, and X. Qiu, "Broad temperature adaptability of vanadium redox flow battery—part 2: cell research," *Electrochimica Acta*, vol. 191, pp. 695–704, 2016.
- [4] S. L. Huang, H. F. Yu, and Y. S. Lin, "Modification of Nafion® membrane via a sol-gel route for vanadium redox flow energy storage battery applications," *Journal of Chemistry*, vol. 2017, Article ID 4590952, 10 pages, 2017.
- [5] L. F. Arenas, C. P. León, and F. C. Walsh, "Mass transport and active area of porous Pt/Ti electrodes for the Zn-Ce redox flow battery determined from limiting current measurements," *Electrochimica Acta*, vol. 221, pp. 154–166, 2016.
- [6] M. Skyllas-Kazacos, M. Rychcik, R. G. Robins, A. G. Fane, and M. A. Green, "New all-vanadium redox flow cell," *Journal of the Electrochemical Society*, vol. 133, no. 5, pp. 1057–1058, 1986.
- [7] A. Parasuraman, T. M. Lim, C. Menictas, and M. Skyllas-Kazacos, "Review of material research and development for vanadium redox flow battery applications," *Electrochimica Acta*, vol. 101, pp. 27–40, 2013.
- [8] J. Maruyama and T. Shinagawa, "Catalyst layer structures for enhancement of redox reactions of V(IV/V) ions," *Electrochimica Acta*, vol. 210, pp. 854–861, 2016.
- [9] L. Wei, T. S. Zhao, G. Zhao, L. An, and L. Zeng, "A high-performance carbon nanoparticle-decorated graphite felt electrode for vanadium redox flow batteries," *Applied Energy*, vol. 176, pp. 74–79, 2016.
- [10] D. Lloyd, T. Vainikka, M. Ronkainen, and K. Kontturi, "Characterisation and application of the Fe(II)/Fe(III) redox reaction in an ionic liquid analogue," *Electrochimica Acta*, vol. 109, pp. 843–851, 2013.
- [11] J. W. Lim and D. G. Lee, "Carbon fiber/polyethylene bipolar plate-carbon felt electrode assembly for vanadium redox flow batteries (VRFB)," *Composite Structures*, vol. 134, pp. 483–492, 2015.
- [12] C. Yang, H. Wang, S. Lu et al., "Titanium nitride as an electrocatalyst for V(II)/V(III) redox couples in all-vanadium redox flow batteries," *Electrochimica Acta*, vol. 182, pp. 834–840, 2015.
- [13] K. Oh, S. Won, and H. Ju, "Numerical study of the effects of carbon felt electrode compression in all-vanadium redox flow batteries," *Electrochimica Acta*, vol. 181, pp. 13–23, 2015.
- [14] G. Nikiforidis, L. Berlouis, D. Hall, and D. Hodgson, "An electrochemical study on the positive electrode side of the zinc–cerium hybrid redox flow battery," *Electrochimica Acta*, vol. 115, pp. 621–629, 2014.
- [15] J. Melke, P. Jakes, J. Langner et al., "Carbon materials for the positive electrode in all-vanadium redox flow batteries," *Carbon*, vol. 78, pp. 220–230, 2014.
- [16] M. L. Chen, S. L. Huang, C. L. Hsieh, J. Y. Lee, and T. J. Tsai, "Development of a novel iodine-vitamin C/vanadium redox flow battery," *Electrochimica Acta*, vol. 141, pp. 241–247, 2014.
- [17] M. H. Pournaghi-Azar and H. Razmi-Nerbin, "Electrocatalytic characteristics of ascorbic acid oxidation at nickel plated aluminum electrodes modified with nickel pentacyanonitrosylferrocate films," *Journal of Electroanalytical Chemistry*, vol. 488, no. 1, pp. 17–24, 2000.
- [18] V. M. Dubin, "Electroless Ni-P deposition on silicon with Pd activation," *Journal of the Electrochemical Society*, vol. 139, no. 5, pp. 1289–1294, 1992.
- [19] B. M. Praveen and T. V. Venkatesha, "Electrodeposition and properties of Zn-nanosized TiO₂ composite coatings," *Applied Surface Science*, vol. 254, no. 8, pp. 2418–2424, 2008.
- [20] J. R. Henry, "Electroless (autocatalytic) plating," *Metal Finishing*, vol. 97, no. 1, pp. 424–435, 1999.
- [21] K. Cheng, D. X. Cao, F. Yang, L. L. Zhang, Y. Xu, and G. L. Wang, "Electrodeposition of Pd nanoparticles on C@TiO₂ nanoarrays: 3D electrode for the direct oxidation of NaBH₄," *Journal of Materials Chemistry*, vol. 22, no. 3, pp. 850–855, 2012.
- [22] F. Hu, F. Ding, S. Song, and P. K. Shen, "Pd electrocatalyst supported on carbonized TiO₂ nanotube for ethanol oxidation," *Journal of Power Sources*, vol. 163, no. 1, pp. 415–419, 2006.
- [23] M. G. Hosseini and I. Ahadzadeh, "A dual-chambered microbial fuel cell with Ti/nano-TiO₂/Pd nano-structure cathode," *Journal of Power Sources*, vol. 220, pp. 292–297, 2012.
- [24] Y. N. Wu, S. J. Liao, H. F. Guo, and X. Y. Hao, "High-performance Pd@PtRu/C catalyst for the anodic oxidation of methanol prepared by decorating Pd/C with a PtRu shell," *Journal of Power Sources*, vol. 224, pp. 66–71, 2013.
- [25] A. J. Bard and L. R. Faulkner, *Electrochemical Methods-Fundamentals and Applications*, Wiley, 2nd edition, 2001.
- [26] S. Li, K. Huang, S. Liu et al., "Effect of organic additives on positive electrolyte for vanadium redox battery," *Electrochimica Acta*, vol. 56, no. 16, pp. 5483–5487, 2011.



Hindawi

Submit your manuscripts at
www.hindawi.com

